https://doi.org/10.1016/j.cemconres.2023.107385

C-S-H decalcification in seawater: the view from the nanoscale

Yong Tao[1], Yining Gao[1], Yanjie Sun[1], Roland J.-M. Pellenq[2,*], Chi Sun Poon[1,*]

[1] Department of Civil and Environmental Engineering, The Hong Kong Polytechnic University, Hung Hom, Kowloon, Hong Kong
[2] Institut Européen des Membranes, CNRS and Université of Montpellier, 300 avenue du Professeur Jeanbrau, 34090 Montpellier, France

Corresponding Authors: roland.pellenq@cnrs.fr (R.J.M.Pellenq); cecspoon@polyu.edu.hk (C.S.Poon)

Abstract

Decalcification of calcium silicate hydrates (C-S-H) is one of the most important issues for cement-based infrastructures concerning long-term safety performance. While enhanced decalcification of C-S-H in saline solution has been extensively characterized by experimental studies, the underlying microscale mechanisms are not well understood. Using molecular simulations with the metadynamics method, we compared the Ca dissolution free energy of amorphous C-S-H and C-S-H-like crystals in pure water and seawater. Previous experimental results were well-explained by our calculations, and we revealed an important mechanism of accelerated C-S-H decalcification in seawater that has not been emphasized before, *i.e.*, the "ion exchange" between surface Ca and electrical double layers in seawater significantly reduces the Ca dissolution free energy through excess entropy gains. This provides a new and sound understanding of decalcification in contrast to previous empirical approaches stating that accelerated decalcification is mainly related to the pore solution's pH value and ionic solubility. It is also found that C-S-H with a larger Ca/Si ratio features lower dissolution free energy. Our finding enhances the assessment and prediction of cementitious materials' degradation and inspires relevant mitigation strategies. This work also enriches the understanding of mineral dissolution with a broader geoscience interest.

Keywords: Thermodynamics; Dissolution; Calcium silicate hydrates; Seawater; Molecular dynamics.

1. Introduction

Ca leaching is one of the most important causes of the deterioration of cement-based constructions, especially when they are under adverse service conditions, such as radioactive waste disposal, underground infrastructure, seawater-mixed concretes, *etc.* [1-3], where cement hydration products are susceptible to multiple chemical attacks by the pore solution species. As Ca leaching proceeds, the porosity of the cementitious materials increases, causing a decrease in strength. Meanwhile, the porosity increase facilitates the permeation of external ions and CO_2, which further accelerates the decalcification of hydration products, leading to materials degradation [4]. Among the numerous Ca-bearing hydration products, portlandite and calcium silicate hydrates (C-S-H) are considered to be the two main sources of Ca leaching in concrete [4]. Generally, portlandite decalcification

proceeds faster than that of C-S-H due to its higher solubility, which makes the decalcification process of C-S-H the rate-controlling step of the long-term Ca leaching of concrete [4, 5].

To eliminate the interference of other hydration products, Glasser *et al.* [6] studied the effect of NaCl solution on the solubility of synthesized C-S-H with different Ca/Si ratios. Relevant studies were also conducted by Hill *et al.* [7-10]. Except for slight discrepancies, the main consistent conclusions are as follows: first, C-S-H decalcification is promoted with the increase of the salt concentration in solution; second, C-S-H with a higher Ca/Si ratio features higher equilibrated calcium concentration, indicating enhanced decalcification; third, Ca leaching is more significant than Si leaching for C-S-H with Ca/Si ratios larger than unity, which implies the non-congruent dissolution of C-S-H; fourth, some foreign ion incorporation (*e.g.*, aluminum) in C-S-H significantly changes the decalcification kinetics and the resulting pore structures. In addition, Barreira *et al.* [11] employed flow-through experiments to calculate the dissolution rate constants of C-S-H and established that the decalcification rate is faster for C-S-H with a higher Ca/Si ratio, exhibiting more pronounced non-congruent dissolution. These conclusions basically agree with those obtained from leaching experiments of cement pastes in ammonium nitrate solution [4, 12-14], which confirms the decalcification process of C-S-H being the rate-controlling step of Ca leaching in cement-based materials.

While the enhanced decalcification of C-S-H in saline solution has been repeatedly confirmed in experiments, the relevant underlying mechanisms are not well understood. Most mechanistic explanations were from the perspectives of porosity, pH, solubility, *etc.* [6, 13-15]. For example, saline solutions may decrease the solution pH and form a more soluble product which promotes C-S-H decalcification. These mechanisms fail to explain the enhanced decalcification of C-S-H in neutral solutions such as NaCl [6, 7]. Moreover, mechanisms concerning the far-from-equilibrium dissolution thermodynamics have not been well demonstrated. Indeed, the nano-scale structural and mechanical evolution of C-S-H has been theoretically studied by manually removing Ca ions from C-S-H[16, 17]. However, the nano-scale insights into the mechanistic picture and energetics of C-S-H decalcification to the best of our knowledge are missing. This is mainly because the free energy cannot be directly measured in the experiment and needs to be estimated by fitting the temperature-dependent kinetic parameters to the Arrhenius law, hence giving the activation energy [12]. Conversely, atomistic simulations are able to directly calculate the free energy by constructing the partition function of a large number of microstates of the system. Then, the reaction kinetics can be further calculated based on the free energy according to the transition state theory [18, 19] or the kinetic Monte Carlo (KMC) methods [20] and directly compared with the experimental data. In this sense, the calculation of free energy is the bridge between experimental research and atomistic simulations. However, in contrast to the well-developed fundamental principles for free energy calculations based on statistical thermodynamics, its implementation in practical atomistic simulations is quite challenging. With realistic computing power and simulation timescales, the system rarely visits high-energy microstates (*e.g.*, transition states), resulting in undersampling for the conformational space. Herein, a series of enhanced sampling techniques have been

developed, such as free energy perturbation [21], umbrella sampling [22], metadynamics [23], *etc.* Among these methods, metadynamics has been highlighted for not requiring an *a priori* reaction pathway since predicting such a reaction pathway for an unknown reaction process is far from trivial.

Applying the state-of-the-art metadynamics scheme, this work unveils the free energy landscape of Ca dissolution from C-S-H gel, the predominant hydration product of Portland cement that governs the main mechanical properties and long-term performance of cement-based constructions. The C-S-H gel in neat Portland cement pastes is typically amorphous, possessing a Ca/Si ratio ranging from 1.2 to 2.3 with a mean value of ~ 1.7 [24]. Experimental evidence has shown that C-S-H with a typical Ca/Si ratio of 1.7 exhibits a non-congruent dissolution mechanism, where Ca species dissolve much faster [25]. This behavior can be attributed to the defective texture of C-S-H at the molecular level, as proposed by Pellenq et al. [26], with interrupted or disrupted silicate chains, allowing intra-layer Ca to directly access the solution near the gel surface or within capillary pores. In contrast, low-Ca/Si-ratio C-S-Hs (e.g., tobermorite crystals) exhibit a congruent dissolution mechanism, wherein Ca and silicate chains dissolve stoichiometrically [11, 25].

This paper focuses specifically on the amorphous C-S-H with a Ca/Si ratio of 1.7. By comparing the thermodynamics of Ca dissolution in pure water and seawater, atomic-level insights into the pore solution effects on C-S-H decalcification are provided and a new mechanism revealing how seawater accelerates the C-S-H decalcification process is unveiled for the first time. Moreover, to simulate C-S-H decalcification under the congruent dissolution scenario, we also constructed surface models of C-S-H-like minerals, *i.e.*, tobermorite and jennite crystals, where the Ca and silicate chains were stoichiometrically removed from supercells layer by layer in the Z direction until the inner Ca layer was exposed to the solution. This procedure preserves the overall system's electroneutrality while also ensuring a surface charge of -0.035 e/nm^2, comparable to that of the tobermorite crystals examined by experiments [27]. While these C-S-H-like crystals are not the primary phases in cement hydrates, their lower Ca/Si ratios make them adequate for gaining a broader understanding of C-S-H decalcification. The calculated free energy data for different C-S-H structures can serve as input parameters for higher-scale simulation methods such as KMC to establish direct correlations with experimental research and facilitate comprehension of the long-term degradation of cementitious materials.

2. Materials and methods

2.1 Molecular simulations on C-S-H decalcification

2.1.1 Models and force fields

C-S-H gel, the main binding component in Portland cement hydration products, is a mixture with extremely complex composition and microstructures. Most of the phases of C-S-H are amorphous colloids, while a few phases exhibit crystalline structures. Among more than 20 C-S-H-like crystals that have been identified in Mineralogy [28, 29], the most representative ones are jennite [30] and three tobermorites [31] with interlayer spacings of 9 Å (T9), 11 Å (T11), and 14 Å (T14) as presented in Fig. 1. In this study, the molecular

structures of T9, T11, T14, and jennite were readily obtained from the Crystallography Open Database. The molecular structure of amorphous C-S-H with an experimentally comparable Ca/Si ratio was not solved for a long time until Pellenq *et al.* [26] constructed the first "realistic" molecular model of C-S-H by a bottom-up atomistic simulation approach. Starting with an 11 Å tobermorite crystal model, Pellenq *et al.* randomly removed charge-neutral SiO_2 groups to promote the Ca/Si ratio and obtain different silica chains (*i.e.*, monomers, dimers, pentamers) based on experimental data. The Grand Canonical Monte Carlo simulations were further performed to adsorb water in the defected dry C-S-H to achieve a reasonable chemical composition and density against experiments. This "realistic" molecular model has been widely adopted to simulate the thermodynamic, reactive, and mechanical properties of C-S-H [32-35]. Moreover, Qomi *et al.* [36] created a C-S-H structure database with various Ca/Si ratios and modified Pellenq *et al.*'s method by adding a reactive force filed [37] optimization to generate reasonable content of hydroxyl groups in C-S-H. We adopted Pellenq and Qomi *et al.*'s approach to construct an amorphous C-S-H model with a typical Ca/Si ratio of ~ 1.7 (Fig. 1).

The unit cells of T9, T11, T14, and jennite in Fig. 1 were duplicated into supercells to obtain a comparable surface size with the amorphous C-S-H model. The surface models of Ca dissolution were built by cleaving the fully relaxed supercell into two slabs with a slit pore width of 40 Å. All amorphous and crystalline C-S-H models share a similar dimension of ~35 Å × 30 Å × 80 Å (*SI Appendix*, Fig. S1). For C-S-H-like crystal models, we tested the slicing positions at the interlayer and intralayer regions. To simulate different conditions, the slit pores of the surface models were filled with either pure water or seawater (*SI Appendix*, Fig. S1). We simulated the seawater solution according to the concentration of the most abundant two cations (Na^+, Mg^{2+}) and one anion (Cl^-) of real seawater as standardized in the literature [38, 39]. The CSH-FF force field [40], which has been widely accepted to calculate the mechanical, surface adsorption, and diffusion properties of C-S-H, was used in this work. For force field parameters and testing results of bulk properties, see *SI Appendix*, Table S2 to S5.

2.1.2 Simulation procedure

All the calculations were carried out with LAMMPS [41] patched with the PLUMED [42] package. The bulk supercells were relaxed under the isothermal-isobaric ensemble (300 K, 0 bar, Nose-Hoover barostat and thermostat) for 10 ns with a timestep of 1 fs before they were adopted to construct the surface models. With the experience in calculating the Ca dissolution of clinker [43], we conducted well-tempered metadynamics [44] with three Cartesian coordinates as the collective variables to unambiguously explore the free energy landscape of Ca dissolution. The width, height, and update frequency of Gaussian potentials were 0.1 Å, 1.5 kJ/mol, and every 150 timesteps, respectively and the bias factor was 20. The metadynamics calculations were performed under the canonical ensemble (300 K, Nose-Hoover thermostat) until the target Ca ion was completely dissolved and became a freely moving ion in the solution. For more information on the metadynamics method, the readers are advised to review the Supporting Information of this paper or papers by Barducci *et al.* [45]. In addition, the detailed information for the calculation of rate

constants and self-diffusion coefficients, as well as the C-S-H dissolution experiments can be found in the Supporting Information.

2.2 Ca leaching experiments of synthesized C-S-H

2.2.1 Materials preparation

Most previous studies on C-S-H dissolution in saline solutions focused on the equilibrium ion concentration over an extended dissolution period (*i.e.*, several months)[5, 6, 25]. While the equilibrium Ca concentration can serve as an indirect indicator of the forward reaction rate constant of the dissolution process, we conducted dissolution kinetics experiments on C-S-H at far-from-equilibrium states to directly verify the theoretical framework of forward reaction free energies and rate constants based on our molecular simulation.

To compare our experimental results with the theoretical predictions, leaching experiments on C-S-H with different Ca/Si ratios in pure water and NaCl solutions were carried out. The C-S-H samples were synthesized via the so-called double decomposition method using $Ca(NO_3)_2$ and Na_2SiO_3 solutions [46]. The Na_2SiO_3 solution was prepared by dissolving 0.1 mole Na_2SiO_3 solid (AR grade, 98%) into 150 mL Milli-Q water. Different concentration $Ca(NO_3)_2$ solutions were prepared by dissolving specific moles of $Ca(NO_3)_2$ solid (AR grade, 99%) into 150 mL Milli-Q water to control the initial Ca/Si ratios between the $Ca(NO_3)_2$ and Na_2SiO_3 solutions. The pH of 150 mL Na_2SiO_3 solution was adjusted to ~13.5 with 10 mol/L NaOH before the slow dropping of 150 mL $Ca(NO_3)_2$ solution with a speed of 2.2 mL/min. The reaction was conducted in a 500 mL beaker in an N_2 glove box with a magnetic stirring speed of 300 rpm for 7 days. The suspension was filtered via a 0.45 μm nylon filter and the solid was washed by ethanol-water (1:1) solution and pure ethanol successively. The washed samples were dried in a vacuum drying box at 40 °C for 7 days before phase analysis and leaching experiments. According to previous studies, the finial Ca/Si of formed C-S-H is lower than the initial Ca/Si design when the C-S-H sample targets a Ca/Si higher than 1.0 [47]. Therefore, we designed the initial Ca/Si ratios of 0.83, 1.0, and 2.2 of raw materials for the target Ca/Si ratios of 0.83, 1.0, and 1.7 of final C-S-H samples.

2.2.2 Leaching experiments and characterization

The C-S-H phase is characterized by X-ray diffraction (XRD) analysis using a Rigaku SmartLab 9 kW diffractometer with a 10 mm slit width and Cu K_α radiation (λ = 1.54 Å). The scanning mode was performed over a 2θ range from 5 ° to 70 ° with a step size of 0.02 ° and a scan rate of 5 °/min. Prior to the XRD measurements, the sample powders underwent a homogenization process and consistency check to ensure uniformity by passing them through a 200-mesh sieve.

The polymerization degree of silicate chains of C-S-H was measured by ^{29}Si solid-state nuclear magnetic resonance (NMR) spectroscopy. The NMR spectrometer apparatus is the Jeol ECZ500R of 500 MHz. The rotational motion of the rotor was maintained at a velocity of 4000 Hz when the data acquisition process employed the well-established magic angle rotation Oneplus technique with a recovery period of 30 seconds. Tetramethylsilane was used as the reference substance for spectrum calibration.

The Ca leaching experiment was conducted by dissolving 1.5 g of C-S-H in 750 g of water in a 900 mL beaker, with a water/solid ratio of 500. The solutions were collected at different time intervals (1, 3, 5, 10, 20, 30, and 60 min), and immediately filtered through a 0.45 μm microporous membrane filter and stored. The Ca ion concentrations in the filtered solutions from different time intervals were determined using an Agilent 5110 Inductively Coupled Plasma Optical Emission Spectrometer (ICP-OES).

3. Results and discussion

3.1 Thermodynamics and kinetics of C-S-H decalcification

In this section, we first reveal the thermodynamic characteristics of Ca dissolution for C-S-H-like crystals, *i.e.*, T9, T11, T14, and jennite and then focus on amorphous C-S-H, whose microstructure and Ca/Si ratio are closer to real cement hydration products. For amorphous C-S-H, we constructed a defected surface structure as close to the realistic C-S-H gel, the calculated Ca dissolution free energy and kinetics are aimed to quantitatively compare with previous experiments and simulations. On the other hand, the simplified surface models were constructed for the C-S-H-like crystals, which do not aim to replicate an authentic C-S-H surface but rather to simulate a scenario of low-Ca/Si-ratio C-S-H structures' decalcification, exhibiting congruent dissolution characteristics. While neglecting the silicate chain residues at the surface, the simplified surface models still retained reasonable negative surface charges, consistent with experimental observations of cement hydrates [27] as aforementioned. Additionally, these models offered a uniform surface complexity, facilitating comparisons among different C-S-H phases and providing clear insights into the interfacial reactions influenced by seawater.

It is worth noting that according to the Terrace-Ledge-Kink model [48, 49], Ca ions at flat surfaces tend to be more stable than those at defected surfaces with edge or kink sites. Thus, the calculated Ca dissolution free energies presented in this study represent the upper limits for each C-S-H-like crystal. Therefore, they are cautiously limited to qualitative comparisons with each other. For the same reason, the free energy comparison between pure water and seawater is also qualitative.

3.1.1 Dissolution of interlayer and intralayer Ca

In the molecular structure of C-S-H, two types of Ca ions can be identified: charge-balancing Ca (interlayer Ca) coordinated with H_2O and/or OH^- groups, and structural Ca (intralayer Ca) that coordinates with the apical oxygen of silicate chains. In the case of amorphous C-S-H, the interlayer and intralayer Ca ions are barely distinguishable and we selected multiple Ca sites to better understand C-S-H decalcification. For C-S-H-like crystals, the intralayer and interlayer Ca ions show much different properties. Fig. 2 compares the dissolution free energies of the intralayer and interlayer Ca ions of T9. Using three Cartesian coordinates as the collective variables, the thermodynamic process of Ca dissolution is explicitly depicted by a three-dimensional free energy landscape. The three Cartesian axes show the displacement of Ca ions in each direction during the dissolution process. Both free energy landscapes show the lowest free energy around the coordinates (0,0,0), indicating that the initial position is the most stable state of Ca ions. As the

dissolution proceeds, the Ca ions detach from their initial sites and gradually access high-energy regions until they are completely dissolved.

In terms of dissolution pathway, the initial dissolution pathway of intralayer Ca is mainly along the *z*-axis, which is understandable because the movement of the surface Ca ions in the *x*- and *y*-axes is confined by the other surface atoms. As the Ca ion slightly detached from the surface, its mobility improves, and the free energy profile thus becomes diffusive. On the contrary, the dissolution pathway of interlayer Ca is much more diffusive from the beginning. The interlayer Ca can laterally move in the *xy* plane without a significant energy barrier to overcome as indicated by the close energy isosurfaces between two neighboring free energy minima. During the dissolution process, the interlayer Ca moves up spirally with much larger displacements in the *xy* plane compared with the intralayer Ca dissolution. This difference of dissolution pathway implies the differences in spatial confinement and ease of decalcification between intralayer and interlayer Ca. The interlayer Ca possesses much weaker or less spatial confinement and thus dissolves much more easily.

Thermodynamically speaking, the dissolution free energy barrier of interlayer Ca is ~20 - 30 kJ/mol, which is a typical level of desorption activation energy of surface adatom [50, 51]. This small free energy barrier ensures the high dissolution reactivity of interlayer Ca, making its content variable in C-S-H, which leads to a change in the Ca/Si ratio (*e.g.*, from T9 to T14) [40]. In contrast, the significantly high dissolution free energy of intralayer Ca guarantees the overall stability of the crystal structure. During the long-term Ca leaching process, the dissolution of intralayer Ca becomes the rate-controlling step for C-S-H-like crystals. Therefore, we focused on the decalcification of intralayer Ca in C-S-H-like crystals for comparison with amorphous C-S-H in the following sections.

3.1.2 Ca dissolution of C-S-H-like crystals

The three-dimensional dissolution free energy landscapes of T9, T11, T14, and jennite are shown in Fig. 3A-H. All free energy landscapes show the lowest free energy around the coordinates (0,0,0), indicating that the initial position is the most stable state of Ca ions. The initial dissolution pathways were narrow and straight in the *z*-direction, which became more diffusive when the Ca ions detached from the surface. Generally, the thermodynamic characteristics of the Ca dissolution in seawater are similar to those in pure water but with lower free energy barriers. The free energy landscapes of the three tobermorite crystals are highly similar and possess a slight *z*-axis symmetry compared to those of jennite. This is because the *c*-axis (the arrangement direction of the layered structure) of the tobermorite crystals is parallel to the *z*-axis of the Cartesian coordinate system while the *c*-axis of the jennite is tilted (Fig. 1). In addition, the free energy landscape of jennite exhibits much more local minima (intermediate states) than that of tobermorite crystals. These intermediate states divide the entire dissolution process with a big free energy barrier into multiple steps with smaller barriers. Although the dissolution process should not be regarded as an integration of independent sequential sub-reactions, the multiple-step scheme increases the probability of reaching the product state compared with the one-big-step mode according to the transition state theory [18, 19]. Jennite in this regard is expected

to have easier decalcification compared with tobermorite crystals, which is confirmed by the dissolution rate constants shown in Fig. 4E.

Based on the free energy landscape, we calculated the free energy profiles along the dissolution path by exploring the minimum energy pathway with the nudged elastic band method [52] (Fig. 3I-L). For the four C-S-H-like crystals, the free energy profiles of Ca dissolution in pure water resemble those in seawater, indicating that Ca dissolution undergoes similar thermodynamic steps regardless of the solution environment. The main difference is that the energy barrier between the initial state (the most stable state) and the first intermediate state in seawater is significantly lower than that in pure water. According to Tao *et al.*'s study on Ca dissolution of clinker crystals, Ca dissolution involves two sequential processes of chemical bond breaking and detachment from the surface [43]. Therefore, Fig. 3I-L shows that seawater species mainly influence the bond-breaking step rather than the desorption step of Ca dissolution. The order of Ca dissolution free energies of the four C-S-H-like crystals in pure water is T9 ≈ T14 > T11 > jennite. While the order does not change in seawater, the free energy barriers are reduced by 11-28 kJ/mol, implying that Ca dissolves more easily in seawater. Vast experiments have confirmed that C-S-H decalcification can be significantly promoted by chemical additives (*e.g.*, NaCl) in the solution [6-8]. While most experimentalists attribute the acceleration effects to the pH and solubility changes [2, 12], our simulations with neutral seawater solution suggest another mechanism of the acceleration effects. The lower dissolution free energy not only indicates a larger forward reaction (*i.e.*, dissolution) rate constant but also suggests a higher equilibrium Ca concentration through the transition state theory, assuming that the free energy barrier of the backward reactions (*i.e.*, nucleation) is similar in both pure water and seawater. Indeed, Glasser *et al.* [6] investigated the long-term dissolution equilibrium of C-S-H with different NaCl solutions. They found that the equilibrated Ca concentration increases with the NaCl concentration in the solution while the pH remains almost constant, which is in good agreement with our calculations and can be well explained by the mechanism demonstrated in Section 3.2.

3.1.3 Ca dissolution of amorphous C-S-H

Compared with the regularly arranged flat surface of C-S-H-like crystals (*SI Appendix*, Fig. S1), the surface of amorphous C-S-H is characterized by multiple atomic defects (Fig. 4A, B). Due to the complex surface topology, we selected four representative Ca sites to calculate Ca dissolution thermodynamics (Fig. 4B). Regardless of the solution environment (pure water or seawater), the Ca dissolution free energy is related to the initial coordination number of Ca ions with surface atoms, *i.e.*, the poorer the coordination with the surface, the smaller the dissolution free energy (Fig. 4C). Compared with C-S-H-like crystals, the Ca dissolution free energy of amorphous C-S-H is generally lower, which means the amorphous C-S-H is easier to decalcify. For each Ca site, the free energy of Ca dissolution in seawater is always lower than that in pure water, which is consistent with the observations in C-S-H-like crystals, reconfirming the effect of seawater species on Ca dissolution. Combining the results of crystalline and amorphous C-S-H, we analyzed the relationship between the Ca dissolution free energy and the Ca/Si ratio of C-S-H (Fig. 4D). The Ca dissolution free energy decreases with the increase of the Ca/Si ratio, which

indicates that C-S-H with a higher Ca/Si ratio is more prone to decalcification. It is in line with Barreira *et al.*'s experiments [11], where an increase in the dissolution rate of C-S-H with higher Ca/Si ratios was observed. Additionally, Harris *et al.*'s experiments showed that C-S-H with higher Ca/Si ratios featured a higher equilibrium Ca concentration [6, 25], providing indirect support for our calculations.

With free energy profiles (Fig. 4D) in hand, the rate constants (Fig. 4E) for the forward dissolution reaction are calculated using the transition state theory[18] (see methods in *SI Appendix*). For all crystalline and amorphous C-S-H models, the Ca dissolution rate constants in seawater are roughly two orders of magnitude higher than in pure water (Fig. 4E), which could lead to accelerated Ca leaching of concrete from decades to months. While quantitative data on the kinetics of seawater-accelerated Ca leaching of C-S-H are lacking in the literature, previous studies reported that the Ca leaching of cement paste in 6 mol/L ammonium nitrate solution could be accelerated by 90 ~ 200 times[4, 12, 14, 53]. Taking into account the Ca ion concentration on the C-S-H surface, the dissolution rate constants of a single Ca ion in Fig. 4E can be converted into the rate constants per unit surface concentration (*SI Appendix*, Table S1). The converted Ca dissolution rate constants of amorphous C-S-H in pure water and seawater are 1.25×10^{-7} and 1.19×10^{-5} $mol\cdot m^{-2}\cdot s^{-1}$, respectively. Considering the dissolution of silicate chains is relatively negligible at this high Ca/Si ratio, the calculated Ca dissolution rate constants are comparable to the C-S-H dissolution rate constants (10^{-7} ~ 10^{-6} $mol\cdot m^{-2}\cdot s^{-1}$) reported by Bullard *et al.* [54-56]. In addition, Barreira *et al.* [11] reported dissolution rate constants ranging from $10^{-7.5}$ to 10^{-11} $mol\ m^{-2}\ s^{-1}$ for C-S-H with Ca/Si ratios ranging from 1.67 to 0.83. Their fitted rate constants were slightly smaller than our calculated values. This difference may be attributed to the higher Ca/Si ratio of our modelled C-S-H, which is 1.7. Besides, they estimated the Ca/Si ratios of C-S-H based on the Ca and Si concentrations in the output solution, which assumed that C-S-H dissolves stoichiometrically. However, this assumption is questionable for C-S-H with higher Ca/Si ratios.

3.1.4 Ca dissolution of C-S-H in experiments

To validate the accelerated decalcification of C-S-H in seawater as indicated by our simulations, we conducted Ca dissolution experiments on synthesized C-S-H samples with varying Ca/Si ratios (Fig. 5). The XRD analyses reveal that all the synthesized C-S-H samples predominantly exhibit amorphous characteristics, with crystallization degrees of approximately 31%, 39%, and 49% for samples with Ca/Si ratios of 0.83, 1.0, and 1.7, respectively. This aligns with the fact that the formation of crystalline tobermorite and jennite requires a significantly longer timeframe. Previous experiments utilizing the double decomposition method also yielded amorphous C-S-H at similar Ca/Si ratios [5]. Although the C-S-H samples are nearly amorphous, their coordination structures differ with respect to Ca/Si ratios (Fig. 5A). In line with earlier experimental studies [57], C-S-H with lower Ca/Si ratios exhibit a higher Q_2/Q_1 ratio, indicating longer silicate chains. This observation is consistent with our simulation models.

Ca dissolution occurs much more rapidly in NaCl solution compared to pure water for all C-S-H samples (Fig. 5C), which is in excellent agreement with our calculations (Fig. 4E).

In addition, it is observed that the higher the Ca/Si ratio, the faster the Ca dissolution of C-S-H in both pure water and NaCl solution. This is consistent with previous studies [6, 11, 25] and supports our earlier calculations.

3.2 Mechanisms of accelerated C-S-H decalcification in seawater

With the knowledge of the differences in Ca dissolution thermodynamics in pure water and seawater, the mechanism of seawater effects needs to be elucidated. Since the Ca dissolution of all C-S-H in seawater undergoes a similar process and the flat surfaces of C-S-H-like crystals are more conducive to capturing the surface reactions, we analyze the seawater ions' behavior on the surface of C-S-H-like crystals to demonstrate its effect on Ca dissolution.

3.2.1 Atomic-scale decalcification process

The Ca dissolution process of the four C-S-H-like crystals in seawater is similar. Taking T9 as an example, Fig. 6 shows the main steps of Ca dissolution in seawater and the corresponding free energy changes. At the very beginning of dissolution, Ca ions were firmly bonded with surface atoms and only made direct contact with 1-2 water molecules (Fig. 6A). Within a short time, a number of cations in the solution were adsorbed to the C-S-H surface and part of them were adsorbed around the target Ca ion (Fig. 6B). As the initial site's restraints to the Ca ion were gradually broken, the Ca ion's coordination number of water was increasing accordingly (Fig. 6G). When the Ca ion detached from the initial site, a pair of Na ions adsorbed nearby approached and occupied the Ca vacancy (Fig. 6C, D). The subsequent process is mainly the Ca desorption from the surface (Fig. 6E, F) with a free energy barrier of ~ 20 kJ/mol (Fig. 6G), which is comparable with previous simulations[58] and experiments[50]. The final coordination number of Ca in the solution is ~ 7, in good agreement with the literature[58]. Since one Na ion is not sufficient to compensate for the negative charge of the Ca vacancy, another Na ion in seawater was adsorbed near the Ca vacancy when the dissolved Ca ion completely diffused into the solution (Fig. 6F). This is interesting because the two Na ions, which are supposed to repel each other, are drawn together due to the strong negatively charged Ca vacancy. The outer Na ion is attracted by a Cl ion and there is no water molecular hydration shell between these adjacent Na ions, making them a "superionic pair", where the electrostatic repulsion between the Na ions is overcome due to the strong interaction with the vacancy (*SI Appendix*, Fig. S2). This superionic state of packing counterions has been observed at the surface of metal/graphene (*i.e.*, electron-conducting) polarized electrodes of supercapacitor devices[59, 60]. It is interesting to note that the super-ionic state is observed here at the defective surface of an insulator giving this concept a more general status that could be related to defect charge localization enhanced by electrical polarization in the case of conducting surfaces.

3.2.2 Formation of the EDL structure

The mechanism of the seawater effect can be qualitatively described according to Fig. 6: for seawater dissolution, numerous cations are rapidly adsorbed on the C-S-H surface to form a positively charged layer before Ca dissolution begins. This layer can timely compensate for the negatively charged Ca vacancy during the Ca dissolution process by

providing cation adsorption (*e.g.*, Na ions), causing an "ion-exchange" behavior, which accelerates the Ca dissolution as described earlier. This mechanism is confirmed by characterizing the formation of the electrical double layer (EDL) structure (Fig. 7) on the C-S-H surface due to seawater ion adsorption. For all seawater ions, their mean square displacement (MSD) slopes along the *x* and *y* axes are comparable and significantly larger than those along the *z*-axis (Fig. 8), indicating that they are all to some extent adsorbed on the C-S-H surface. As the Ca dissolution proceeds, the MSD slope of Na ions declines the fastest and the final slope is the lowest, which suggests that Na ions feature the fastest and strongest adsorption on the surface of C-S-H. The MSD slope of Cl ion is the largest, implying that Cl ion is the most diffusive among the three species. The density distributions of different seawater ions along the *z*-axis direction also show that although all ions exhibit surface adsorption, the adsorption of anions is much weaker (*SI Appendix*, Fig. S3), which results in the formation of a classical EDL Stern structure on the C-S-H surface (Fig. 7), *i.e.*, a positively charged stern layer (~ 3 Å thick) formed by firmly adsorbed cations and a negatively charged diffuse layer formed by loosely adsorbed anions. The EDL structure has been widely observed experimentally in cementitious materials [61]. Therefore, the effect of seawater to accelerate Ca dissolution lies in the "ion exchange" between surface Ca ions and EDL. It is worth noting that the Stern layer is mainly contributed by Na ions rather than Mg ions, which is mainly ascribed to two aspects. First, the Mg concentration in seawater is much lower than that of Na ions (Mg/Na ≈ 1:6 in the seawater models). Secondly, the water exchange rate of Na ions is much larger than that of Mg ions [62], leading to higher mobility of Na ions in solution.

3.2.3 Excess entropy gain from EDL formation

With free energy in hand from metadynamics calculations, the entropy change is also readily available (Fig. 9), which provides a more in-depth understanding of the effect of the formed EDL. For pure water and seawater systems, both internal energy and entropy increase with the Ca dissolution, the former being the resistance while the latter being the driving force. The dashed lines in Fig. 9 locate the critical position (~ 3 Å above the surface) where the Ca ion is about to leave the surface, beyond which the calculation of configurational entropy becomes difficult and free energy is unavailable. In the seawater system, this critical position is also roughly the boundary between the Stern and diffuse layers of the EDL structure (Fig. 7). The internal energy and entropy changes at the critical position show that the "ion exchange" at the EDL in seawater promotes the internal energy gain by ~10 kJ/mol while favors the entropy gain by ~13.2 kJ/mol compared to the pure water system. The latter overpowers the former to account for the net decrease of Ca dissolution free energy in seawater. In other words, the excess entropy gain from the formation of EDL in seawater is the overwhelming driving force that accelerates the C-S-H decalcification. When increasing the concentration of seawater ions, both internal energy and entropy gains increased, and the free energy of Ca dissolution further decreased (Fig. 9E). This further supports the entropy-driven EDL effect of seawater and also agrees with the Ca leaching acceleration of C-S-H with the salinity of the solution as observed in experiments [6].

3.3 Further discussion on the nature of Ca dissolution

For the free energy calculations of Ca dissolution, it should be noted that most free energy calculation methods, including metadynamics, are not adequate for the accurate calculation of configurational entropy of ions in solution, because the conformational space converts from a localized dissolution site to the entire solution region after the ions dissociate from the surface, which cannot be adequately sampled on the common simulation timescales. Therefore, these methods are not capable of a complete dissolution free energy profile, at the end of which a continuous entropy increase should be expected, leading to free energy decay [63, 64]. However, the absence of the free energy tail merely prohibits our knowledge of the energy barrier for the reverse reaction (*i.e.*, nucleation), and the energy barrier for the forward dissolution reaction is still reliable.

The dissolution free energy is contributed by both enthalpy (or internal energy for NVT ensembles) and entropy changes. The entropy gain is usually true for a dissolution process as the configurational entropy of Ca ions in solution is much greater than that at the surface, whereas the changes in internal energy depend on the sum of the endothermic dissociation process and the exothermic solvation process. Taking T9 as an example, Ca dissolution in both pure water and seawater leads to a growth in the internal energy (Fig. 10). As the Ca ion tries to escape from the initial site for an entropy gain, the Coulomb interactions from the negatively charged Ca vacancy keep attracting Ca back against the internal energy gain. This competition dominates the free energy barrier for Ca dissolution. Following this mechanism, the dissolution free energy for the second Ca ion increased dramatically and the dissolution rate decreased by 5 orders of magnitude due to the charge effect of the previous Ca vacancy (Fig. 11). However, for real Ca leaching from C-S-H in hardened concrete, the accumulative charge effect of Ca vacancies would be considerably alleviated by counterion adsorption or surface reconfiguration, which leads to the decline of the Ca leaching rate in a mild way.

4. Conclusions

In this work, the nanoscale decalcification process and thermodynamics of crystalline and amorphous C-S-H in pure water and seawater were uncovered for the first time. Based on the dissolution free energy calculations with advanced rare-event sampling techniques, previous experimental results were well-explained, and we revealed an important mechanism of accelerated C-S-H decalcification in seawater that has not been emphasized before. The main conclusions and limitations of this work are as follows.

For a specific C-S-H surface, the more coordination numbers (chemical bonds) of Ca ions with the surface at the initial site, the higher the dissolution free energy. Amorphous C-S-H possesses a higher Ca/Si ratio and poorer coordination numbers of surface Ca ions than C-S-H-like crystals, and it thus has a lower Ca dissolution free energy.

The Ca dissolution free energy in seawater is ~ 20 kJ/mol lower than that in pure water, which accelerates the dissolution rate constants by two orders of magnitude. Unlike most experimental studies that attribute the accelerated C-S-H decalcification to the pH value and ionic solubility in solution, we unveiled another mechanism thanks to the EDL structure. The seawater ions rapidly form the EDL structure on the C-S-H surface, within

which the adsorbed cations can timely compensate for the charges of Ca vacancy to induce the "ion exchange" between the surface Ca of C-S-H and nearby seawater cations. Compared to the Ca dissolution in pure water, this "ion exchange" process in seawater enhances the internal energy gain by ~10 kJ/mol while benefiting the entropy gain by ~13.2 kJ/mol. The latter overwhelms the former to account for the net decrease of Ca dissolution free energy in seawater.

As more and more Ca ions dissolve from the surface, the cumulative charge effect of Ca vacancies, if not alleviated by ion adsorption or surface reconfiguration, will boost the free energy barrier for Ca dissolution and thus lead to a rapid decline in the dissolution rate. This might explain the leaching depth being proportional to the square root of time as observed experimentally.

The comparison between crystalline and amorphous C-S-H suggests that C-S-H structures with higher Ca/Si ratios exhibit lower dissolution free energy, leading to more susceptible decalcification, which aligns well with our experimental results and previous studies. However, since the crystalline C-S-H surface models utilized in this work are simplified and our primary focus lies on the seawater effect, further exploration of the underlying mechanisms explaining the relationship between Ca/Si ratios and decalcification thermodynamics has not been extensively pursued in this study. Future research efforts are expected to delve deeper into this aspect.

Acknowledgments

The authors extend their sincere gratitude to Dr. Ali Morshedi for his valuable assistance in constructing the amorphous C-S-H model. The work described in this paper is supported by the Theme-Based Research Scheme of the Research Grants Council of the Hong Kong SAR Government (Project No. T22-502/18-R), and the Start-up Fund for RAPs under the Strategic Hiring Scheme (Project ID: P0045160).

CRediT authorship contribution statement

Y.T.: Conceptualization, Methodology, Investigation, Formal analysis, Writing – original draft, Writing – review & editing; **Y.G.**: Investigation, Formal analysis; **Y.S.**: Investigation, Formal analysis; **R.J.-M.P**: Supervision, Writing – review & editing; **C.S.P**: Supervision, Writing – review & editing.

Declaration of competing interest

The authors declare no conflict of interest.

Data availability

Data will be made available on request.

Appendix A. Supplementary data

Supplementary information: SI Appendix

References

[1] Y. Sun, Y.L. Yaphary, C.S. Poon, Experimental and mesoscale simulation studies of micro-mechanical properties of alite mixed with NaCl solutions, Cement and Concrete Research, 159 (2022).
[2] Y.J. Du, M.L. Wei, K.R. Reddy, Z.P. Liu, F. Jin, Effect of acid rain pH on leaching behavior of cement stabilized lead-contaminated soil, J Hazard Mater, 271 (2014) 131-140.
[3] Y. Cai, Y. Tao, D. Xuan, Y. Sun, C.S. Poon, Effect of seawater on the morphology, structure, and properties of synthetic ettringite, Cement and Concrete Research, 163 (2023) 107034.
[4] K. Wan, Y. Li, W. Sun, Experimental and modelling research of the accelerated calcium leaching of cement paste in ammonium nitrate solution, Construction and Building Materials, 40 (2013) 832-846.
[5] X. Liu, P. Feng, X. Yu, J. Huang, Decalcification of calcium silicate hydrate (C-S-H) under aggressive solution attack, Construction and Building Materials, 342 (2022).
[6] F.P. Glasser, J. Pedersen, K. Goldthorpe, M. Atkins, Solubility reactions of cement components with NaCl solutions: I. Ca(OH)2 and C-S-H, Advances in Cement Research, 17 (2005) 57-64.
[7] J. Hill, A.W. Harris, M. Manning, A. Chambers, S.W. Swanton, The effect of sodium chloride on the dissolution of calcium silicate hydrate gels, Waste Manag, 26 (2006) 758-768.
[8] D. Sugiyama, Chemical alteration of calcium silicate hydrate (C–S–H) in sodium chloride solution, Cement and Concrete Research, 38 (2008) 1270-1275.
[9] M. Jin, Y. Ma, W. Li, J. Huang, Y. Yan, H. Zeng, C. Lu, J. Liu, Multi-scale investigation on composition-structure of C-(A)-S-H with different Al/Si ratios under attack of decalcification action, Cement and Concrete Research, 172 (2023) 107251.
[10] S.-Y. Hong, F.P. Glasser, Alkali sorption by C-S-H and C-A-S-H gels: Part II. Role of alumina, Cement and Concrete Research, 32 (2002) 1101-1111.
[11] A. Trapote-Barreira, J. Cama, J.M. Soler, Dissolution kinetics of C–S–H gel: Flow-through experiments, Physics and Chemistry of the Earth, Parts A/B/C, 70-71 (2014) 17-31.
[12] Y. Yu, Y.X. Zhang, Coupling of chemical kinetics and thermodynamics for simulations of leaching of cement paste in ammonium nitrate solution, Cement and Concrete Research, 95 (2017) 95-107.
[13] J. Jain, N. Neithalath, Analysis of calcium leaching behavior of plain and modified cement pastes in pure water, Cement and Concrete Composites, 31 (2009) 176-185.
[14] S. Kamali, M. Moranville, S. Leclercq, Material and environmental parameter effects on the leaching of cement pastes: Experiments and modelling, Cement and Concrete Research, 38 (2008) 575-585.
[15] K. Haga, S. Sutou, M. Hironaga, S. Tanaka, S. Nagasaki, Effects of porosity on leaching of Ca from hardened ordinary Portland cement paste, Cement and Concrete Research, 35 (2005) 1764-1775.
[16] Y. Zhang, L. Guo, J. Shi, Q. Luo, J. Jiang, D. Hou, Full process of calcium silicate hydrate decalcification: Molecular structure, dynamics, and mechanical properties, Cement and Concrete Research, 161 (2022).
[17] Y. Liang, Nanoscale insight into structural characteristics and dynamic properties of C-S-H after decalcification by reactive molecular dynamics simulations, Materials Today Communications, 33 (2022) 104684.
[18] J.E. Straub, D.A. Hsu, B.J. Berne, On determining reaction kinetics by molecular dynamics using absorbing barriers, The Journal of Physical Chemistry, 89 (1985) 5188-5191.
[19] W.H. Miller, Quantum mechanical transition state theory and a new semiclassical model for reaction rate constants, The Journal of Chemical Physics, 61 (1974) 1823-1834.
[20] P. Martin, H. Manzano, J.S. Dolado, Mechanisms and dynamics of mineral dissolution: A new kinetic Monte Carlo model, Advanced Theory and Simulations, 2 (2019) 1900114.
[21] R.W. Zwanzig, High-temperature equation of state by a perturbation method. I. Nonpolar gases, The Journal of Chemical Physics, 22 (1954) 1420-1426.
[22] G. Torrie, J. Valleau, Monte Carlo study of a phase-separating liquid mixture by umbrella sampling, The Journal of Chemical Physics, 66 (1977) 1402-1408.

[23] A. Laio, M. Parrinello, Escaping free-energy minima, Proceedings of the National Academy of Sciences, 99 (2002) 12562.
[24] I.G. Richardson, The nature of C-S-H in hardened cements, Cement and Concrete Research, 29 (1999) 1131-1147.
[25] A.W. Harris, M.C. Manning, W.M. Tearle, C.J. Tweed, Testing of models of the dissolution of cements—leaching of synthetic CSH gels, Cement and Concrete Research, 32 (2002) 731-746.
[26] R.J.-M. Pellenq, A. Kushima, R. Shahsavari, K.J. Van Vliet, M.J. Buehler, S. Yip, F.-J. Ulm, A realistic molecular model of cement hydrates, Proceedings of the National Academy of Sciences, 106 (2009) 16102-16107.
[27] S. Diamond, W. Dolch, J.L. White, Studies on tobermorite-like calcium silicate hydrates, Highway Research Record, (1964).
[28] C. Dharmawardhana, M. Bakare, A. Misra, W.-Y. Ching, Nature of interatomic bonding in controlling the mechanical properties of calcium silicate hydrates, Journal of the American Ceramic Society, 99 (2016) 2120-2130.
[29] W. Kurdowski, Cement and concrete chemistry, Springer Science & Business2014.
[30] E. Bonaccorsi, S. Merlino, H.F.W. Taylor, The crystal structure of jennite, Ca9Si6O18(OH)6·8H2O, Cement and Concrete Research, 34 (2004) 1481-1488.
[31] S. Merlino, E. Bonaccorsi, T. Armbruster, Tobermorites: Their real structure and order-disorder (OD) character, American Mineralogist, 84 (1999) 1613-1621.
[32] A. Morshedifard, S. Masoumi, M.J. Abdolhosseini Qomi, Nanoscale origins of creep in calcium silicate hydrates, Nature Communications, 9 (2018) 1785.
[33] M.J. Abdolhosseini Qomi, F.-J. Ulm, R.J.M. Pellenq, Physical origins of thermal properties of cement paste, Physical Review Applied, 3 (2015) 064010.
[34] M.J.A. Qomi, M. Bauchy, F.-J. Ulm, R.J.-M. Pellenq, Anomalous composition-dependent dynamics of nanoconfined water in the interlayer of disordered calcium-silicates, The Journal of Chemical Physics, 140 (2014) 054515.
[35] M. Bauchy, M.J. Qomi, F.J. Ulm, R.J. Pellenq, Order and disorder in calcium-silicate-hydrate, The Journal of Chemical Physics, 140 (2014) 1-11.
[36] M.J. Abdolhosseini Qomi, K.J. Krakowiak, M. Bauchy, K.L. Stewart, R. Shahsavari, D. Jagannathan, D.B. Brommer, A. Baronnet, M.J. Buehler, S. Yip, F.J. Ulm, K.J. Van Vliet, R.J. Pellenq, Combinatorial molecular optimization of cement hydrates, Nature Communications, 5 (2014) 4960.
[37] H. Manzano, S. Moeini, F. Marinelli, A.C. van Duin, F.J. Ulm, R.J. Pellenq, Confined water dissociation in microporous defective silicates: Mechanism, dipole distribution, and impact on substrate properties, Journal of the American Chemical Society, 134 (2012) 2208-2215.
[38] A.S.f. Testing, Materials, Standard practice for the preparation of substitute ocean water, ASTM International2013.
[39] Y. Cai, D. Xuan, P. Hou, J. Shi, C.S. Poon, Effect of seawater as mixing water on the hydration behaviour of tricalcium aluminate, Cement and Concrete Research, 149 (2021).
[40] R. Shahsavari, R.J. Pellenq, F.J. Ulm, Empirical force fields for complex hydrated calcio-silicate layered materials, Physical Chemistry Chemical Physics, 13 (2011) 1002-1011.
[41] S. Plimpton, Fast parallel algorithms for short-range molecular dynamics, Journal of Computational Physics, 117 (1995) 1-19.
[42] M. Bonomi, D. Branduardi, G. Bussi, C. Camilloni, D. Provasi, P. Raiteri, D. Donadio, F. Marinelli, F. Pietrucci, R.A. Broglia, M. Parrinello, PLUMED: A portable plugin for free-energy calculations with molecular dynamics, Computer Physics Communications, 180 (2009) 1961-1972.
[43] Y. Tao, S. Zare, F. Wang, M.J.A. Qomi, Atomistic thermodynamics and kinetics of dicalcium silicate dissolution, Cement and Concrete Research, 157 (2022).
[44] A. Barducci, G. Bussi, M. Parrinello, Well-tempered metadynamics: A smoothly converging and tunable free-energy method, Physical Review Letters, 100 (2008) 020603.

[45] A. Barducci, M. Bonomi, M. Parrinello, Metadynamics, Wiley Interdisciplinary Reviews: Computational Molecular Science, 1 (2011) 826-843.
[46] A. Kumar, B.J. Walder, A. Kunhi Mohamed, A. Hofstetter, B. Srinivasan, A.J. Rossini, K. Scrivener, L. Emsley, P. Bowen, The Atomic-Level Structure of Cementitious Calcium Silicate Hydrate, The Journal of Physical Chemistry C, 121 (2017) 17188-17196.
[47] Z. Hu, M. Wyrzykowski, M. Griffa, K. Scrivener, P. Lura, Young's modulus and creep of calcium-silicate-hydrate compacts measured by microindentation, Cement and Concrete Research, 134 (2020) 106104.
[48] I.N. Stranski, Zur theorie des kristallwachstums, Zeitschrift für physikalische Chemie, 136 (1928) 259-278.
[49] W. Kossel, Extenoling the law of bravais, Nach. Ges. Wiss. Gottingen, 143 (1927) 25.
[50] J.O. Agbenin, B. van Raij, Rate processes of calcium, magnesium and potassium desorption from variable-charge soils by mixed ion-exchange resins, Geoderma, 93 (1999) 141-157.
[51] S. Kerisit, C. Liu, E.S. Ilton, Molecular dynamics simulations of the orthoclase (001)- and (010)-water interfaces, Geochimica et Cosmochimica Acta, 72 (2008) 1481-1497.
[52] G. Henkelman, H. Jónsson, Improved tangent estimate in the nudged elastic band method for finding minimum energy paths and saddle points, The Journal of Chemical Physics, 113 (2000) 9978-9985.
[53] C. Carde, R. François, Effect of the leaching of calcium hydroxide from cement paste on mechanical and physical properties, Cement and Concrete Research, 27 (1997) 539-550.
[54] J.W. Bullard, R.J. Flatt, New Insights Into the Effect of Calcium Hydroxide Precipitation on the Kinetics of Tricalcium Silicate Hydration, Journal of the American Ceramic Society, 93 (2010) 1894-1903.
[55] J.W. Bullard, E. Enjolras, W.L. George, S.G. Satterfield, J.E. Terrill, A parallel reaction-transport model applied to cement hydration and microstructure development, Modelling and Simulation in Materials Science and Engineering, 18 (2010) 025007.
[56] J.W. Bullard, A determination of hydration mechanisms for tricalcium silicate using a kinetic cellular automaton model, Journal of the American Ceramic Society, 91 (2008) 2088-2097.
[57] Y. Chiang, S.-W. Chang, Bridging the gap between NMR measured mean silicate chain length and nano-scale silicate polymorphism of calcium silicate hydrates, Cement and Concrete Research, 140 (2021).
[58] P. Raiteri, R. Demichelis, J.D. Gale, Thermodynamically consistent force field for molecular dynamics simulations of alkaline-earth carbonates and their aqueous speciation, The Journal of Physical Chemistry C, 119 (2015) 24447-24458.
[59] Y. Groda, M. Dudka, A.A. Kornyshev, G. Oshanin, S. Kondrat, Superionic Liquids in Conducting Nanoslits: Insights from Theory and Simulations, J Phys Chem C Nanomater Interfaces, 125 (2021) 4968-4976.
[60] S. Kondrat, A. Kornyshev, Superionic state in double-layer capacitors with nanoporous electrodes, Journal of Physics: Condensed Matter, 23 (2011) 022201.
[61] E. Nägele, The zeta-potential of cement, Cement and Concrete Research, 15 (1985) 453-462.
[62] L. Helm, A.E. Merbach, Water exchange on metal ions: experiments and simulations, Coordination Chemistry Reviews, 187 (1999) 151-181.
[63] D. Gebauer, P. Raiteri, J.D. Gale, H. Cölfen, On classical and non-classical views on nucleation, American Journal of Science, 318 (2018) 969.
[64] A. Silvestri, P. Raiteri, J.D. Gale, Obtaining consistent free energies for ion binding at surfaces from solution: Pathways versus alchemy for determining kink site stability, Journal of chemical theory and computation, (2022).

Figures

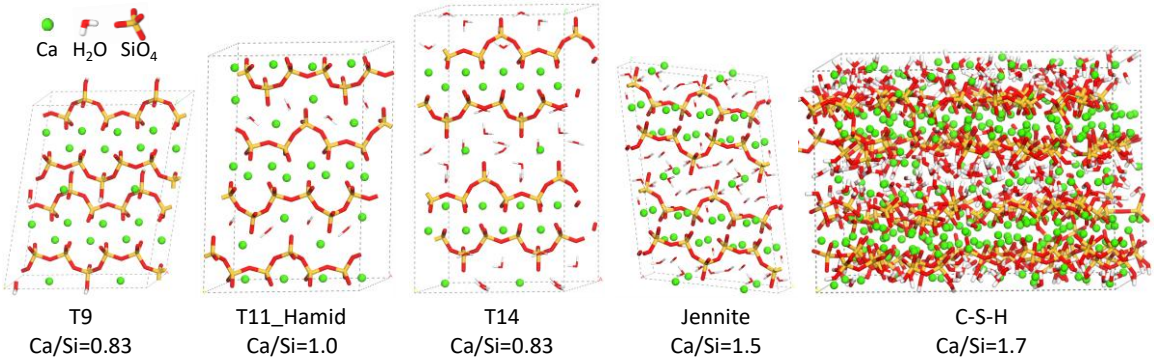

Fig. 1 Unit cells of T9, T11(of Hamid), T14, and jennite crystals, and amorphous C-S-H with of Ca/Si ratio of 1.7.

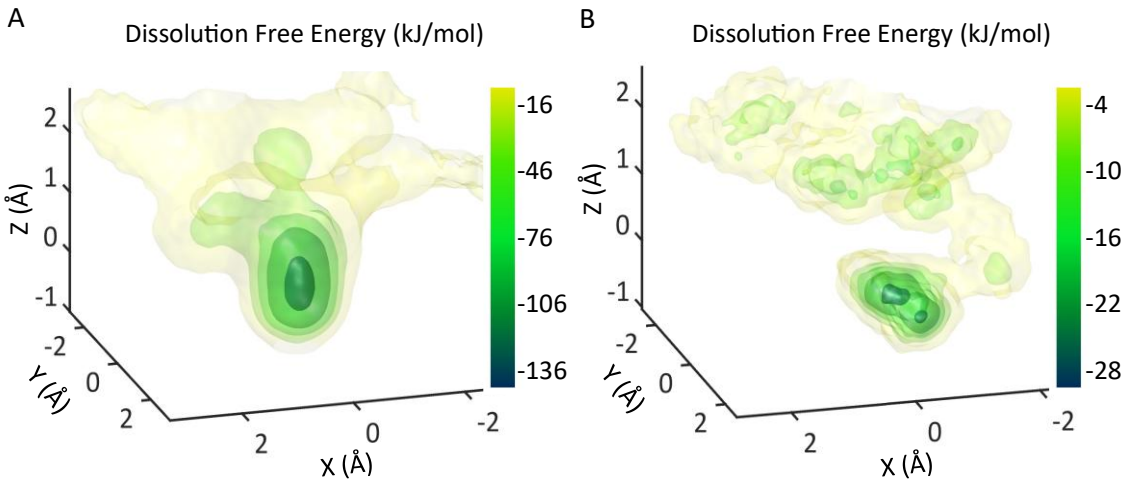

Fig. 2 Dissolution free energy of intralayer (A) and interlayer (B) Ca of T9 in pure water. The three Cartesian axes show the displacement of Ca ions in each direction during the dissolution process. The interlayer Ca features a significantly lower dissolution free energy barrier than that of the intralayer Ca.

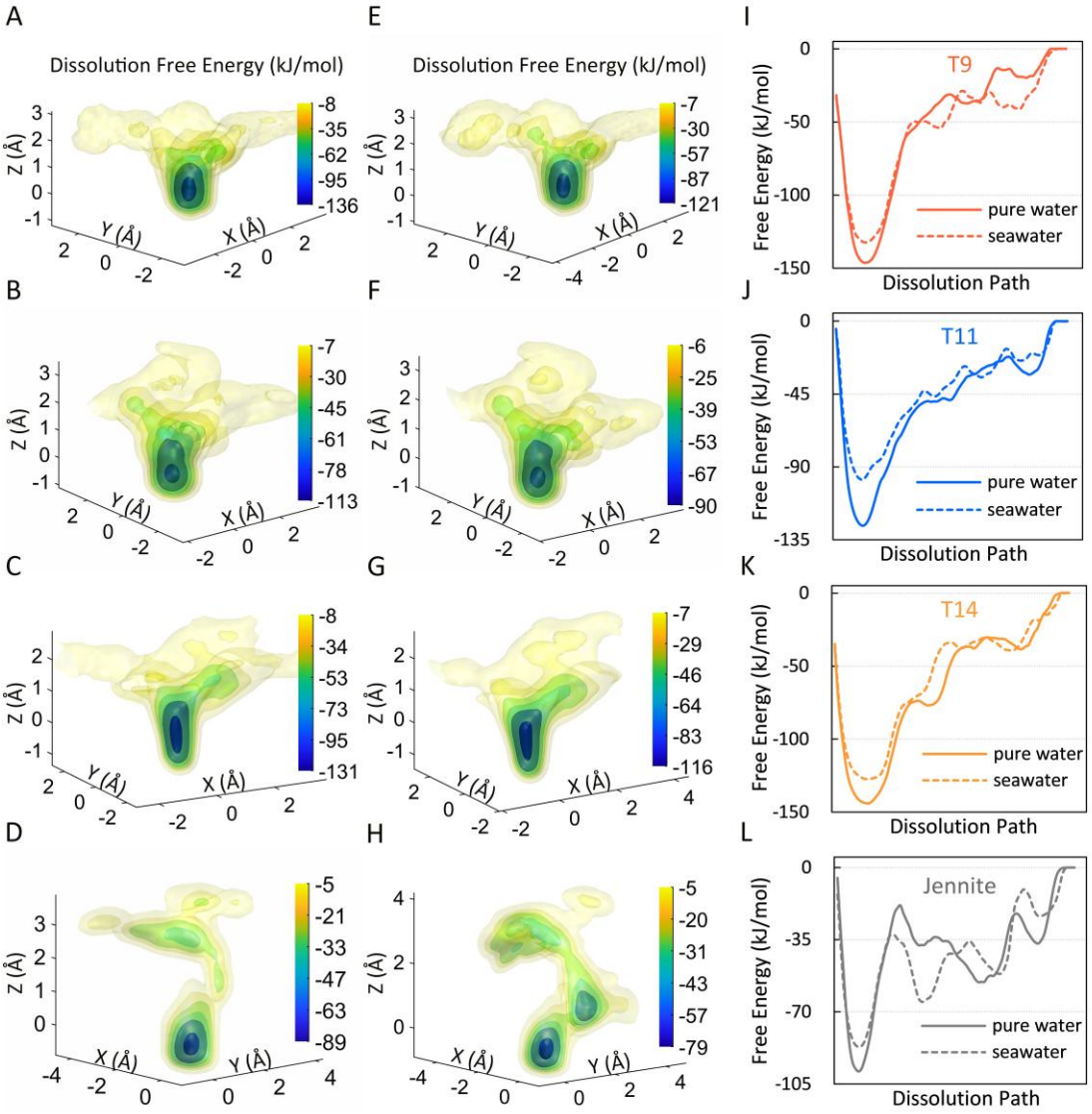

Fig. 3 Ca dissolution free energy of T9, T11, T14, and jennite in pure water and seawater. Three-dimensional free energy landscapes of Ca dissolution for the four crystals in pure water (A-D) and seawater (E-H). The three Cartesian axes show the displacement of Ca ions in each direction during the dissolution process. Based on the free energy landscapes, the free energy profiles along the minimum energy pathway are explored (I-L).

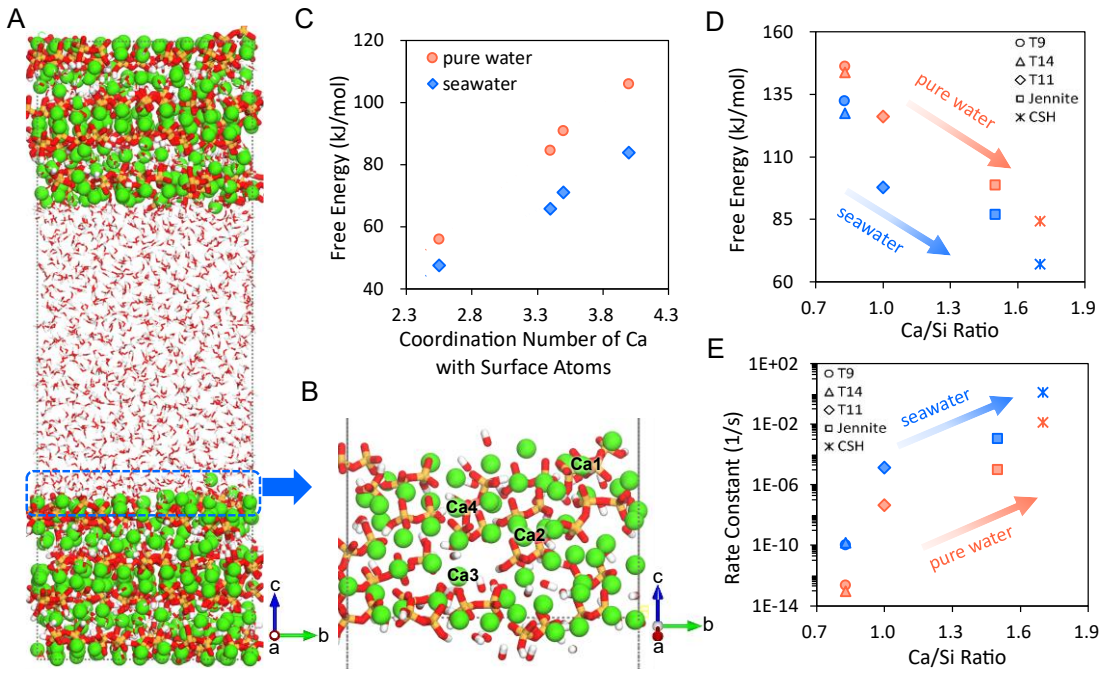

Fig. 4 Ca dissolution free energy of amorphous C-S-H (A-C) and the Ca/Si ratio related thermodynamics and kinetics (D, E): (A) The Ca dissolution model of amorphous C-S-H; (B) Atom arrangement of the disordered surface with four selected representative Ca sites; (C) Dissolution free energy of selected Ca sites on the amorphous C-S-H surface in pure water and seawater; (D) Ca dissolution free energy and (E) rate constants against the Ca/Si ratios of different types of C-S-H. The label "CSH" in panels (D) and (E) denotes the amorphous C-S-H, whose free energy is the average of the four sites in panel (C).

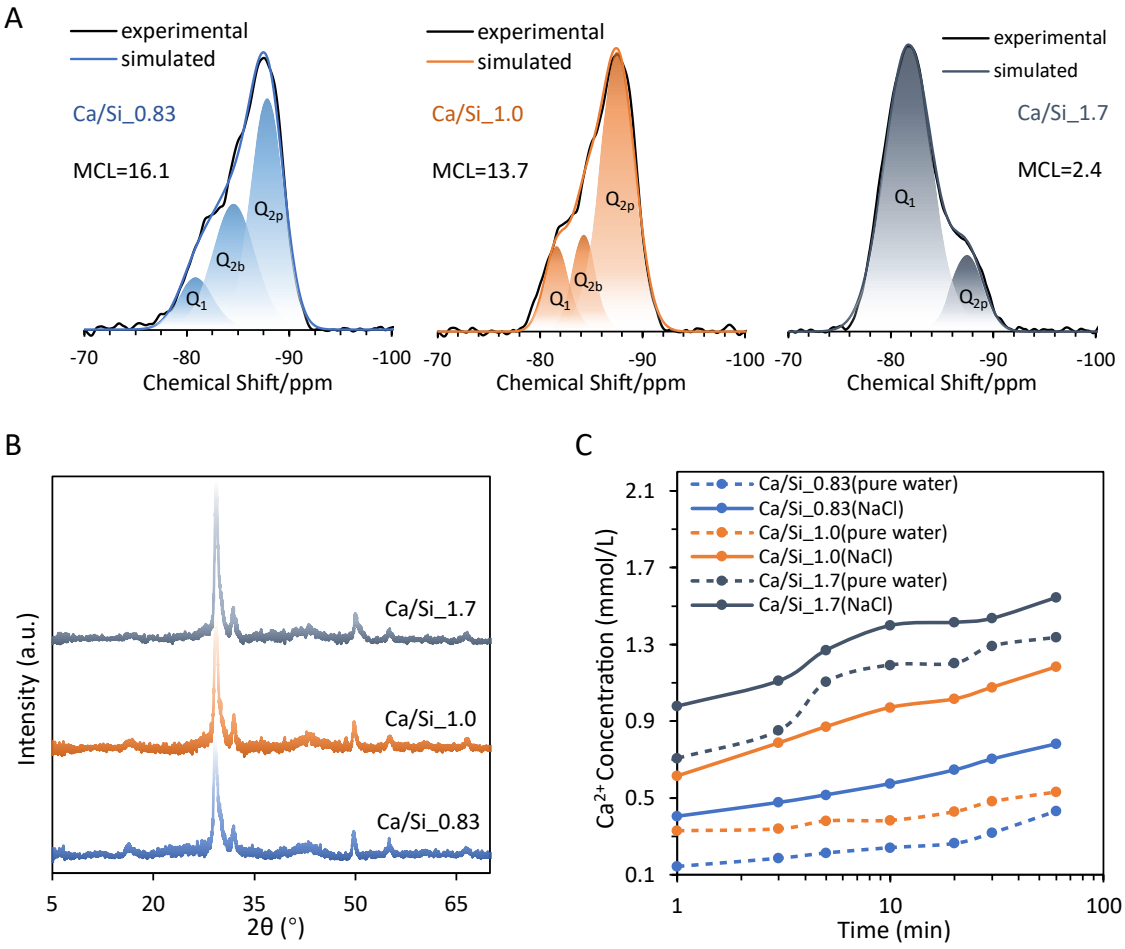

Fig. 5 Structure characterization of synthesized C-S-H samples with different Ca/Si ratios (0.83, 1.0, and 1.7) and their dissolution experiments. (A) ^{29}Si NMR spectra of different C-S-H. The mean silicate chain length (MCL) of each C-S-H sample is calculated from the content of Q_1 and Q_2. (B) XRD patterns of different C-S-H. (C) Ca concentrations in solution as a function of leaching time for different C-S-H exposed in pure water and NaCl solution. The Ca concentrations in NaCl solutions are consistently higher than those in the pure water groups during the initial hour of the Ca leaching process.

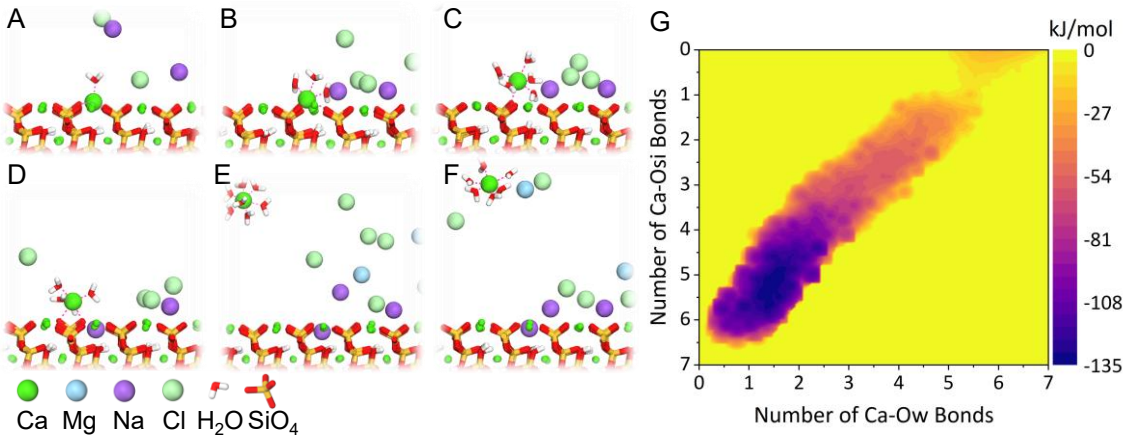

Fig. 6 Snapshots of the Ca dissolution process of T9 in seawater (A-F) and the dissolution free energy map as a function of Ca coordination numbers (G). The green spheres represent Ca ions and the sphere for the dissolved Ca ion is magnified. Water molecules in the solution are hidden for clarity except those coordinated with the dissolved Ca ion. The Ca-Ow and Ca-Osi bonds denote the chemical bonds of Ca with water oxygen and silicate oxygen respectively.

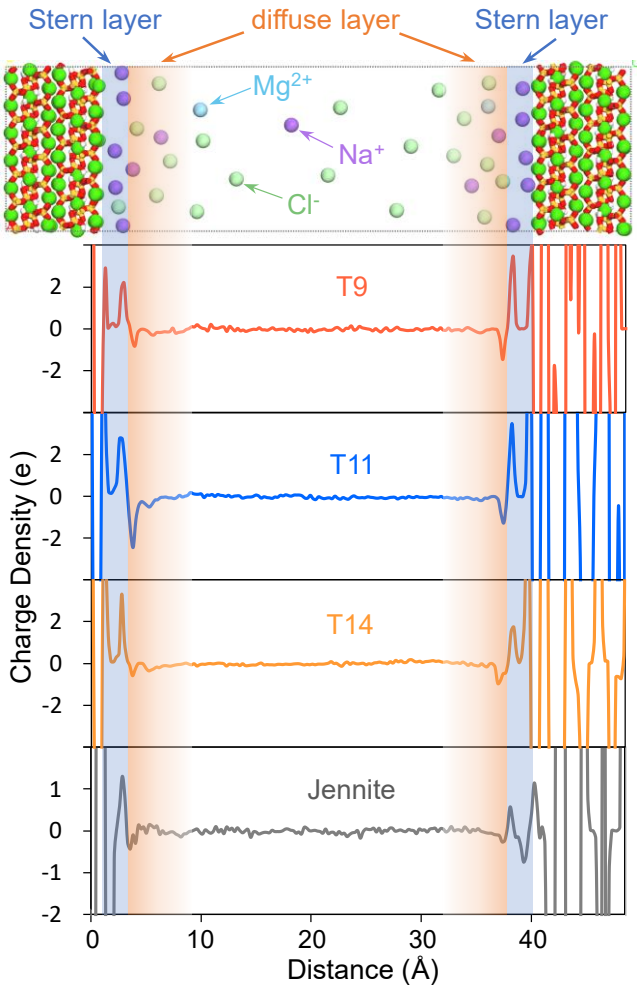

Fig. 7 Charge density distributions of seawater solution in the *z*-axis direction for T9, T11, T14, and jennite. The electrical double layer structures are observed near the C-S-H surfaces with the firmly adsorbed cations forming the stern layer and the loosely adsorbed anions forming the diffuse layer.

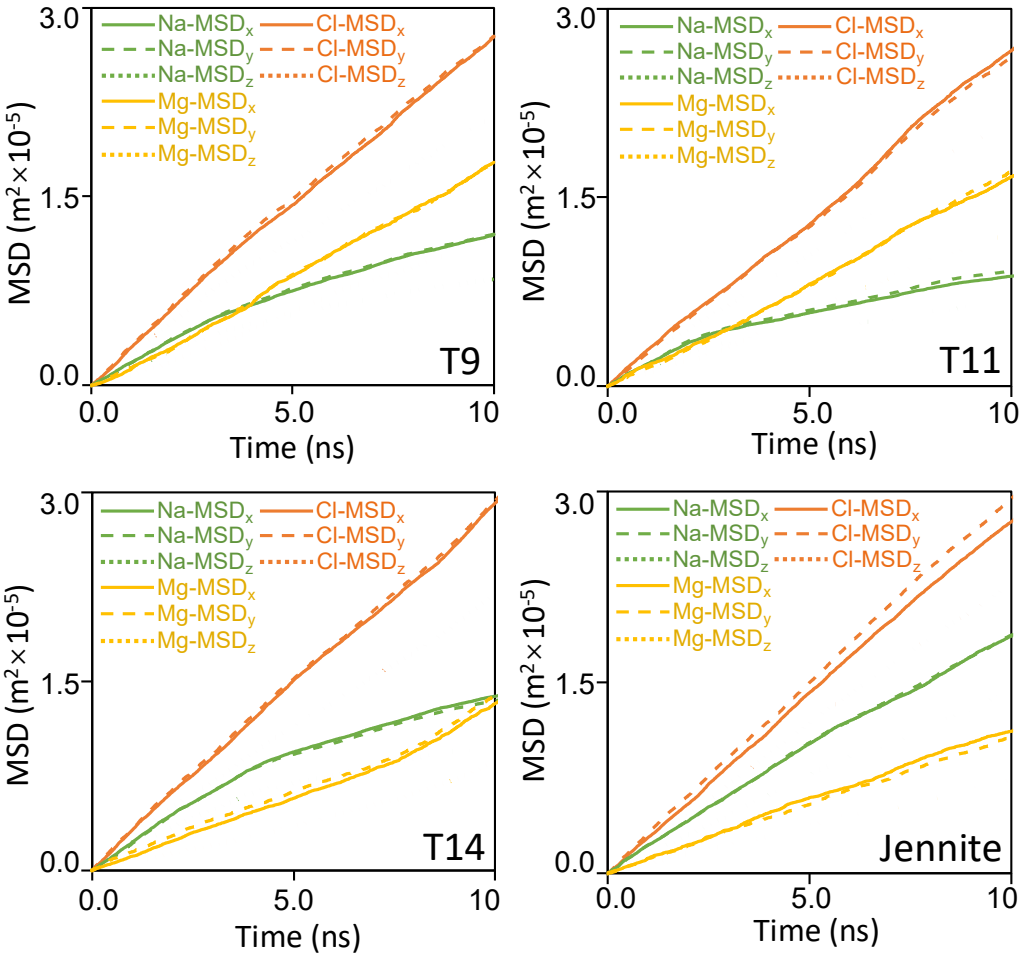

Fig. 8 Time-dependent mean square displacement (MSD) of seawater species during the Ca dissolution process for T9, T11, T14, and jennite. The MSD in *x*, *y*, and *z* directions, *i.e.*, MSD_x, MSD_y, and MSD_z are calculated respectively.

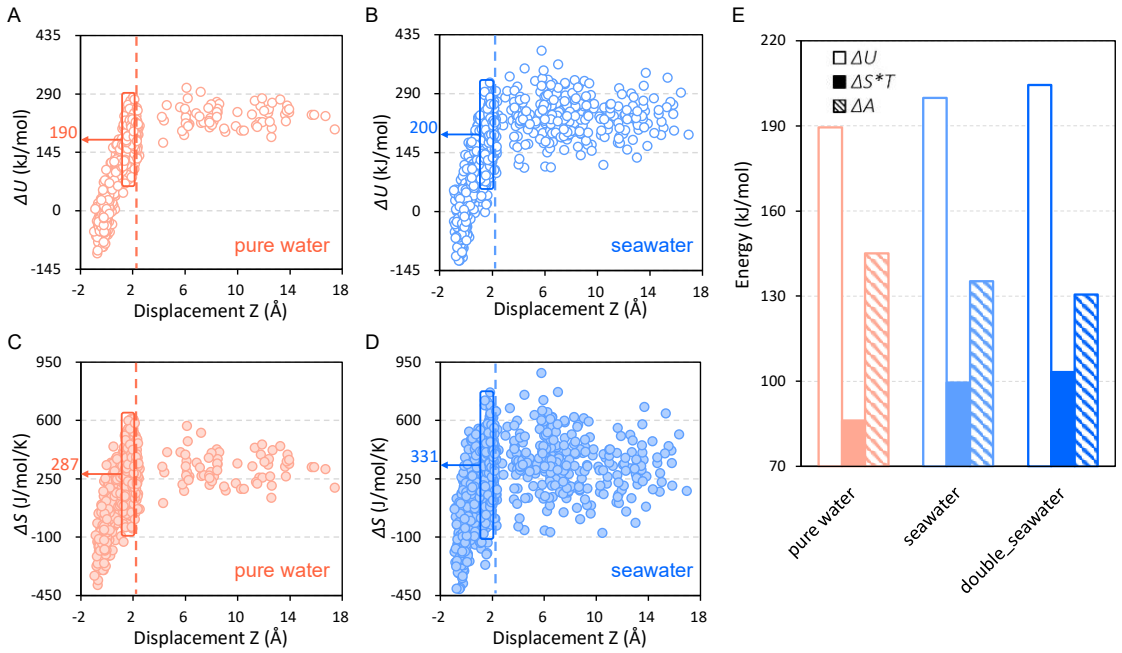

Fig. 9 Internal energy and entropy changes as a function of Ca dissolution in the Z direction for T9: Internal energy changes in pure water (A) and seawater (B); Entropy changes in pure water (C) and seawater (D). The internal energy changes due to Ca dissolution are mainly localized and barely perceptible relative to the thermal fluctuations of the entire system. Hence, the calculations of internal energy and entropy here focused on the dissolved Ca and ions neighboring the Ca vacancy. For the seawater system, Na, Cl, and Mg ions were also considered because their adsorption near the Ca vacancy actively contributed to the internal energy and entropy changes. The dashed lines locate the critical positions where the diffusion process starts. The internal energy and entropy changes at the critical position are presented by averaging, which are further compared for different systems, *i.e.*, pure water, seawater, and double seawater (twice the seawater ion concentration) (E). The free energy barriers are for the whole Ca dissolution process while the internal energy and entropy changes are for the dissolution process at the critical positions.

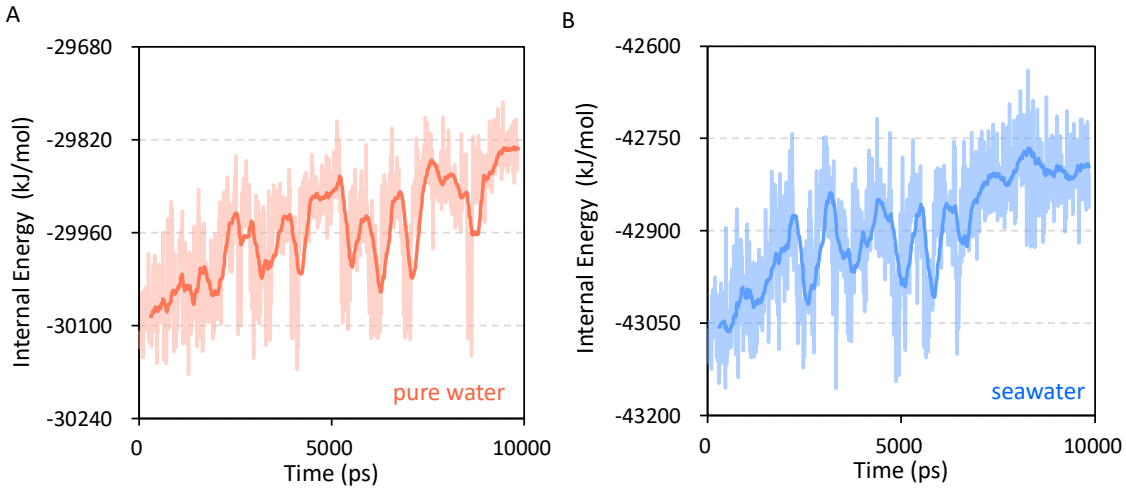

Fig. 10 Internal Energy evolution during the Ca dissolution process for T9. For the pure water system (A), the internal energy calculation involved the dissolved Ca ion and atoms neighboring the Ca vacancy. For the seawater system (B), the internal energy additionally included the seawater species, i.e., Na, Mg, and Cl ions. The darker lines show the moving average.

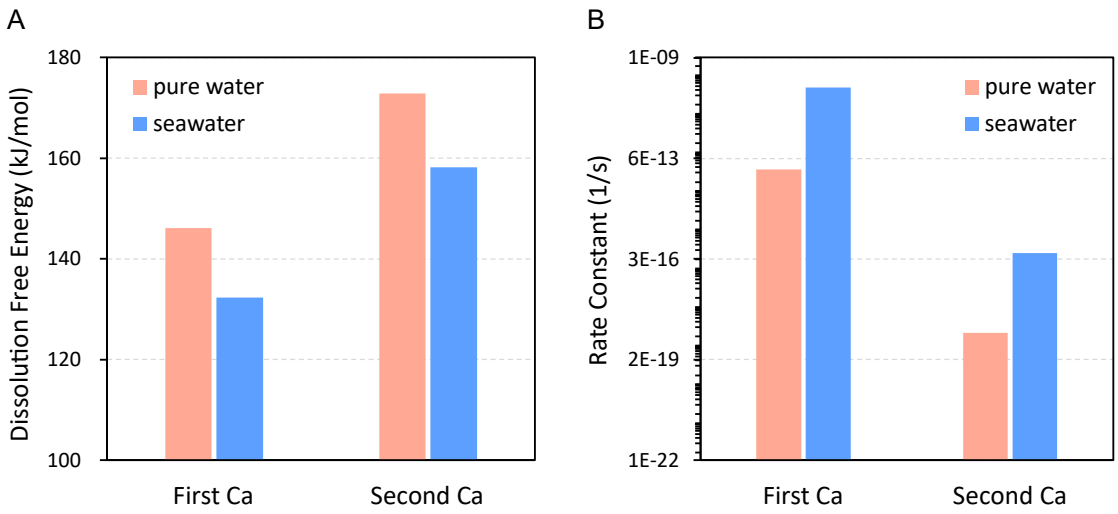

Fig. 11 Comparison of the first and second Ca ions dissolution of T9 in pure water and seawater: (A) dissolution free energies and (B) dissolution rate constants.